Results in Engineering 25 (2025) 104575

Contents lists available at ScienceDirect

Results in Engineering

journal homepage: www.sciencedirect.com/journal/results-in-engineering

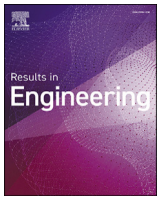

Research paper

Topology optimization of broadband polarization conversion metasurfaces in microwave region

Honglin Zhong [a,b], Bowen Li [c], Yu Lin [c], Yeming Han [c], Chengmiao Wang [c], Wei Sha [a,*], Jan G. Korvink [d,*], Yongbo Deng [d,*]

[a] Changchun Institute of Optics, Fine Mechanics and Physics (CIOMP), Chinese Academy of Sciences, Changchun 130033, China
[b] University of Chinese Academy of Sciences, Beijing 100039, China
[c] State Key Laboratory of Applied Optics (SKLAO), Changchun Institute of Optics, Fine Mechanics and Physics (CIOMP), Chinese Academy of Sciences, Changchun 130033, China
[d] Institute of Microstructure Technology (IMT), Karlsruhe Institute of Technology (KIT), Hermann-von-Helmholtzplatz 1, 76344 Eggenstein-Leopoldshafen, Germany

ARTICLE INFO

Keywords:
Metasurfaces
Polarization conversion
Broadband
Topology optimization

ABSTRACT

Polarization conversion metasurfaces are compact and efficient devices that manipulate the polarization state of electromagnetic waves, offering significant advantages in applications such as antennas, imaging systems, and optical communication. Traditional design methods often struggle to achieve high polarization conversion efficiency across wide bandwidths. To overcome this limitation, we present a gradient-based topology optimization method that uses material distribution approach for the design of broadband polarization conversion metasurfaces. In the broadband optimization process, we adopt a max-min-type objective function, where multiple frequency points within a given frequency band are selected, and the minimum objective value among them is maximized to ensure that the optimized structure performs effectively across the entire frequency range. We applied this method to the inverse design of polarization conversion metasurfaces targeting the X-band, Ku-band, K-band, and Ka-band. Our results demonstrate that the metasurfaces achieve polarization conversion ratios exceeding 90% across these broad frequency bands, significantly enhancing their bandwidth performance. Experimental validation was performed to verify the topologically optimized metasurfaces, where the measured results exhibit remarkable agreement with their numerical counterparts. This approach offers a powerful tool for the design of broadband polarization conversion metasurfaces and holds great promise for various applications, including frequency-selective surfaces, absorbing metasurfaces, and other advanced electromagnetic devices.

1. Introduction

Polarization is a fundamental property of electromagnetic waves (EM waves), describing the orientation of the oscillating electric field vector. In many practical applications, converting the polarization state of waves is crucial for improving the performance of devices, e.g., antennas, imaging systems, and optical communication systems [1–5]. In recent years, polarization conversion metasurfaces have garnered significant attention due to their ability to manipulate EM waves with compact and planar structures [6–13]. By precisely controlling the phase shift and amplitude of the reflected or transmitted wave, polarization conversion metasurfaces can achieve highly efficient polarization transformations. Such metasurfaces are increasingly being integrated into various optical and microwave devices, where they enable several novel functionalities, e.g., polarization-sensitive imaging, multi-functional antennas, polarization multiplexed devices, polarization control, RCS reduction, and multifunctional microstrip array [6,9–11,14–19].

Most of the current design methods for polarization conversion metasurfaces rely on heuristic approaches, guided by the experience and intuition of the designer [12,20–24]. Intuition based design methods usually involve trial-and-error procedures or rely on analytical models to predict the behavior of the metasurfaces. For example, designers can adjust the shape, orientation and size of the unit cells of the metasurfaces to achieve the desired polarization conversion effect across a broad range of frequencies. Although those approaches have been successfully applied, they face significant challenges on designing metasurfaces for broad bandwidths [24–26]. This is because that it is challenging to achieve high efficiency in a wide operating bandwidth. The interaction

* Corresponding authors.
E-mail addresses: yongbo.deng@kit.edu (Y. Deng), jan.korvink@kit.edu (J.G. Korvink), 13756883069@163.com (W. Sha).

https://doi.org/10.1016/j.rineng.2025.104575
Received 4 January 2025; Received in revised form 26 February 2025; Accepted 4 March 2025
Available online 7 March 2025

between the incident wave and the metasurface is highly dependent of the geometry of the unit cells. Therefore, tuning the geometries of the unit cells for broadband operation is complex and time-cost. Along with the increase of the demand for high-performance polarization conversion devices, the limitations of the intuition based design methods have become more apparent. This prompts the exploration of alternative design strategies.

To overcome the limitations of the intuition based design methods, optimization algorithms have been introduced to implement the inverse design of metasurfaces. Lin et al. implemented inverse design of polarization-insensitive, large-area, and high-numerical-aperture monolithic metalenses through an optimization framework based on rigorous coupled-wave analysis [27]; Wang et al. demonstrated that incorporating the performance evaluation of geometrically eroded and dilated structures into iterative optimization algorithms can enhance the robustness of topology optimization of metasurfaces [28]; Wu et al. innovatively integrated an explicit equivalent circuit intervention model into an implicit deep learning methodology to guide metasurface design and thereby circumvent the computationally intensive approaches [29]. As one of the inverse design methods, genetic algorithms based topology optimization method have been used by some researchers to design polarization conversion metasurfaces [21,30–32]. These algorithms typically rely solely on the objective function values, which make them be conveniently used as black-box optimization tools. However, the limited information provided by the objective function values, combined with the random strategies used to update the design variables, makes those algorithms less efficient for the optimization problems involving a large number of design variables [33]. Due to the limitation in the number of design variables, structures obtained using genetic algorithms often exhibit a noticeable checkerboard pattern associated point connection issues [21,30–32,34]. This requires high fabrication precision and may even lead to performance instability when the device is used in practice [34,35]. Topology optimization method with gradient-based optimization techniques, implemented by the material distribution approach, can easily handle problems with a large number of design variables, where the gradient of the objective function contains a substantial amount of information. The gradient information can greatly accelerate the iteration process, and it can be computed efficiently by using the solutions of the associated adjoint equations [36–40].

This article devotes to the gradient-based topology optimization carried out by material distribution approach for the design of polarization conversion metasurfaces. Compared to the existing genetic algorithms reported in the literatures which typically handle around 100 design variables [21,30–32], our developed method achieves a substantial increase in the design variables number up to 2500. This significant enhancement benefits from the superior capability of gradient-based algorithms in managing problems with a large number of design variables, thereby offers more design freedom compared to the existing genetic algorithms. The problem formulation is based on Maxwell's equations, discretized by using the finite element method (FEM). The method of moving asymptotes (MMA) is used to update the design variables. To validate the effectiveness of this method, we present numerical examples and experimental verification for different target frequency bands and further analyze the broadband conversion mechanism of the topologically optimized metasurfaces through theoretical analysis based on surface current distributions. The principal symbols used in this article are shown in Table 1, and the key points of this article are shown in Table 2.

Table 1
Principal Symbols and Definitions.

Symbols	Definition
Operator	
∇	gradient operator in Cartesian coordinate system
$\nabla_{\mathbf{x}'}$	gradient operator in the PML with transformed coordinates
$\cdot$	inner product operator
$*$	conjugate operator of a complex variable
Electromagnetic field relevant variables and parameters	
E_i	incident electric field
E_r	reflected (or scattered) electric field
E	total electric field
E_{ind}	induced electric field
H_{ind}	induced magnetic field
ω	angular frequency
m	magnetic dipole moment
ϕ	phase
λ	wavelength
k	wave vector
α	wavenumber
j	imaginary unit
t	time
R_{xx}	co-polarized reflection coefficients
R_{yx}	cross-polarized reflection coefficients
Material and dimensional parameters	
ε_r	relative permittivity
μ_r	relative permeability
σ	conductivity
ε_0	vacuum permittivity
μ_0	vacuum permeability
p	unit period
h	dielectric layer thickness
Optimize relevant variables and parameters	
ρ	design variable
ρ_f	filtered design variable
ρ_e	elementwised design variable
ρ_p	projected design variable
r	filter radius,
ξ	projection point
β	projection slope
J	objective function
N	total number of mesh elements used to discretize the design domain

Table 2
Key Points of the Article.

No.	Key Points
1	A novel polarization conversion metasurface design method based on topology optimization is presented.
2	The rational design space for the unit period and dielectric thickness of polarization conversion metasurfaces is studied.
3	Four broadband polarization conversion metasurfaces are inversely designed for different target frequency bands. Within the target operating frequency bands, the PCR of the metasurfaces consistently exceeds 90% which has been experimentally verified. Additionally, the mechanism of broadband polarization conversion is further investigated.

2. Method

2.1. Polarization conversion

Fig. 1a is the sketch of the unit cell for a polarization conversion metasurface. The metasurface extends infinitely in the xOy-plane with a period size of p. Consider the incident wave as a plane wave traveling in the $-z$ direction, with its electric field oriented along the x-axis, the front plane of the metasurface is illuminated vertically as illustrated in Fig. 1. The incident electric field can be expressed as

$$\mathbf{E_i} = E_0 e^{jk_0 z}\hat{\mathbf{u}}_\mathbf{x} \tag{1}$$

where E_0 is the amplitude of the incident wave, $k_0(=2\pi/\lambda_0)$ is the free space wavenumber, λ_0 is the free space wavelength, and $\hat{\mathbf{u}}_\mathbf{x}$ is the unit vector along the x axis.

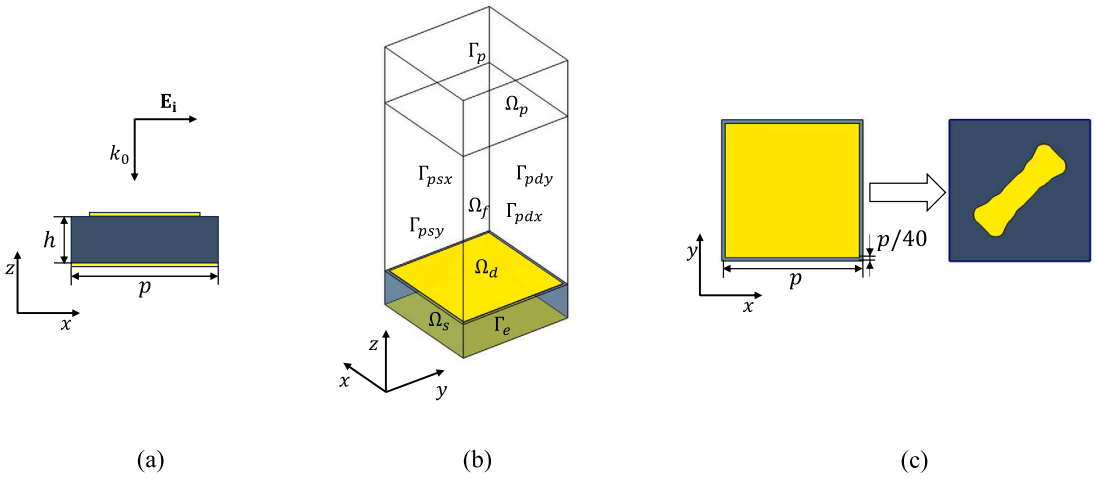

(a) (b) (c)

Fig. 1. (a) Sketch of the unit cell for the polarization conversion metasurfaces, where $\mathbf{E}_i$ is incident field, k_0 is freespace wavenumber, p is period of unit cell and h is d dielectric thickness; (b) sketch for the three-dimensional FEM model of the unit cell, consists of the PML domain Ω_P, free space domain Ω_f, substrate domain Ω_s and design domain Ω_d for metal patch located on the top of the substrate, where Γ_e is external boundary of the unit cell, Γ_p is external boundary of PML, Γ_{psx} and Γ_{psy} are source boundary of the periodic boundary pair, and Γ_{pdx} and Γ_{pdy} are destination boundary of the periodic boundary pair; (c) sketch for topology optimization of the metal patch. The design domain is separated from the unit cell boundary by a distance of $p/40$ to prevent adhesion between adjacent cells.

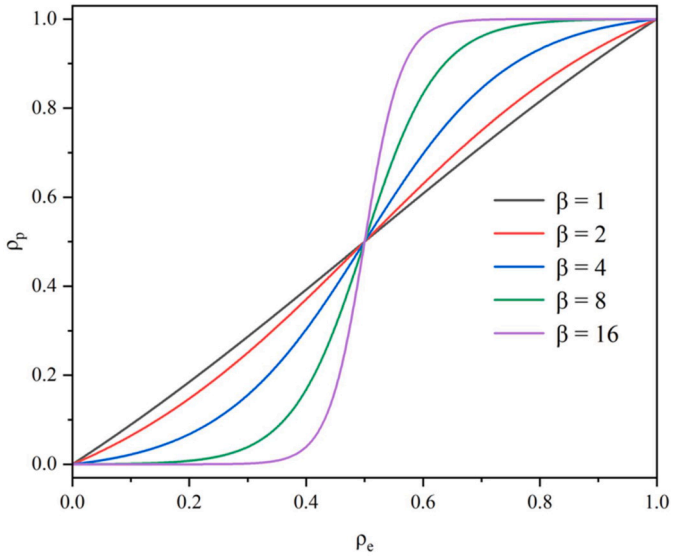

Fig. 2. Heaviside function.

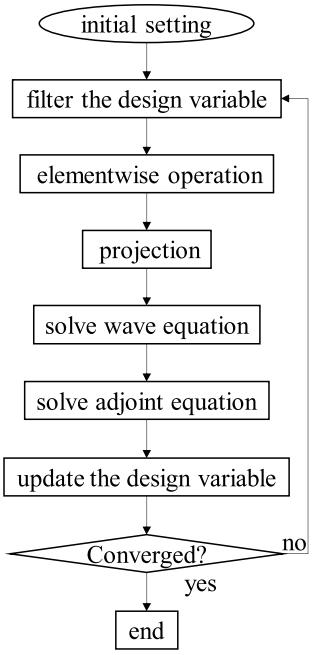

Fig. 3. Flowchart for the iterative solution of the topology optimization problem.

Due to the periodicity of the metasurface along the x axis and the y axis, the reflected electric field can be expressed as a doubly infinite series of Floquet harmonics:

$$\mathbf{E}_r = E_o \sum_m^{\infty} \sum_n^{\infty} \left\{ (R_{xx}^{m,n}\hat{\mathbf{u}}_\mathbf{x} + R_{yx}^{m,n}\hat{\mathbf{u}}_\mathbf{y}) e^{\left[\frac{j(mx+ny)2\pi}{p}\right]} e^{(-j\alpha^{m,n}z)} \right\} \tag{2}$$

where the wavenumbers $\alpha^{m,n}$ can be expressed as

$$\alpha^{m,n} = \sqrt{k_0^2 - \left(\frac{2\pi}{p}\right)^2 (m^2 + n^2)}; \tag{3}$$

$R_{xx}^{m,n}$ and $R_{yx}^{m,n}$ are co-polarized reflection coefficients (x to x) and cross-polarized reflection coefficients (x to y), respectively; and $\hat{\mathbf{u}}_\mathbf{x}$ and $\hat{\mathbf{u}}_\mathbf{y}$ are the unit vectors along the x axis and y axis, respectively.

Based on different values of m and n, the reflection coefficient in equation (2) can be categorized into specular and non-specular reflections. Specifically, when $m = 0$ and $n = 0$, the reflection coefficient corresponds to the specular reflection of the electric field. For the other values of m and n, the reflection coefficient represents non-specular reflection. Non-specular reflection is primarily caused by the excitation of higher-order modes, with characteristics closely related to the operating frequency and incident angle of the EM wave [41]. Therefore, assuming that the loss of EM waves in the substrate is neglected, when the electric field vertically illuminates the front plane of the metasurface, the reflected electric field can be expressed as

$$\mathbf{E}_\mathbf{r} \to E_0(R_{xx}\hat{\mathbf{u}}_\mathbf{x} + R_{yx}\hat{\mathbf{u}}_\mathbf{y}) e^{-jk_0\mathbf{z}} \tag{4}$$

as $z \to \infty$, with $m = 0$ and $n = 0$. The degree of cross-polarization conversion of the reflected electric field can be measured by the polarization conversion ratio (PCR), which can express as

$$\mathrm{PCR} = \frac{\left|R_{yx}\right|^2}{\left|R_{xx}\right|^2 + \left|R_{yx}\right|^2} \in [0, 1]. \tag{5}$$

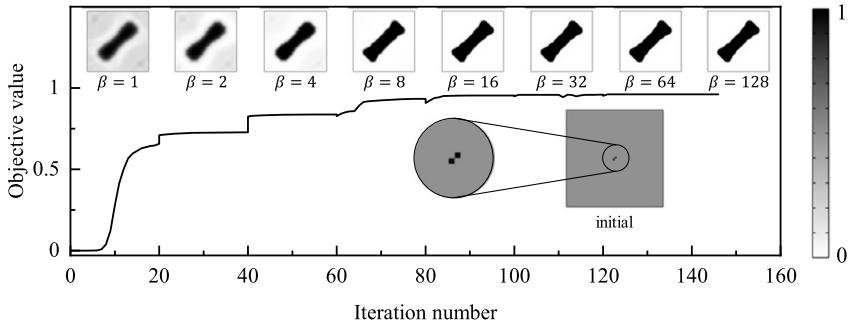

Fig. 4. Iteration history of the metasurface targeting the X-band.

2.2. Wave propagation model

The three-dimensional model is considered as shown in Fig. 1b. The computational domain is set to be a unit cell of the polarization conversion metasurface. The unit cell follows a typical sandwich structure [42,43], consisting of a dielectric substrate, a metal patch on top, and a metallic ground plane at the bottom to fully reflect EM waves. The dielectric material is selected as FR4 (flame retardant-4), which is chosen for its low loss characteristics, with the relative dielectric constant $\varepsilon_r = 4.5$ and conductivity $\sigma = 0.004 S/m$.

The time-harmonic electric field distribution within the computational domain is determined by solving the three-dimensional Maxwell's equations expressed as

$$\begin{aligned} &\nabla \times [\mu_r^{-1} \nabla \times (\mathbf{E}_r + \mathbf{E}_i)] - k_0^2 (\varepsilon_r - \frac{j\sigma}{\omega \varepsilon_0})(\mathbf{E}_r + \mathbf{E}_i) = 0, \text{in } \Omega \\ &\nabla \cdot [(\varepsilon_r - \frac{j\sigma}{\omega \varepsilon_0})(\mathbf{E}_r + \mathbf{E}_i)] = 0, \text{in } \Omega \end{aligned} \quad (6)$$

The formulation of equation (6) employs a Cartesian coordinate system with ∇ denoting the gradient operator; to mitigate dispersion errors, a scattering-field decomposition is adopted, where the total electric field is expressed as $\mathbf{E} = \mathbf{E}_r + \mathbf{E}_i$, comprising the scattered field $\mathbf{E}_r$ and incident field $\mathbf{E}_i$ [44]. The material properties are characterized by relative permittivity ε_r, relative permeability μ_r, and conductivity σ. Here, $k_0 = \omega\sqrt{\varepsilon_0 \mu_0}$ represents the free-space wavenumber, where ω is angular frequency, ε_0 and μ_0 denote vacuum permittivity and permeability respectively. All fields exhibit harmonic time dependence governed by the factor $e^{j\omega t}$, with $j = \sqrt{-1}$ denoting the imaginary unit and t representing the time. The divergence-free nature of Maxwell's equations is inherently preserved through the use of edge elements in FEM [45]. The perfect electric conductor (PEC) condition, $\mathbf{n} \times (\mathbf{E}_r + \mathbf{E}_i) = 0$, is enforced on surface Γ_e to model complete electromagnetic wave reflection at the metallic ground plane, where $\mathbf{n}$ is the outward-pointing unit normal vector at the domain boundary. To truncate the infinite computational space, perfectly matched layer (PML) is used to absorb the outgoing waves and prevent the spurious reflections from the boundaries of the computational domain [46], which is implemented by solving the wave equations with the complex-valued coordinate transformation [47]

$$\nabla_{\mathbf{x}'} \times (\mu_r^{-1} \nabla \times \mathbf{E}_r) - k_0^2 \varepsilon_r \mathbf{E}_r = 0, \text{in } \Omega_P \quad (7)$$

where $\mathbf{x}'$ is the complex-valued coordinate transformed from the original Cartesian coordinate in Ω_P; $\nabla_{\mathbf{x}'}$ is the gradient operator in the PML with transformed coordinates; the transformed coordinates and the original Cartesian coordinates satisfy the transformation

$$\begin{aligned} &\mathbf{x}' = \mathbf{T}\mathbf{x}, \forall \mathbf{x} \in \Omega_P \\ &\mathbf{T} = \begin{pmatrix} 1 & 0 & 0 \\ 0 & 1 & 0 \\ 0 & 0 & (1-j)\lambda/d \end{pmatrix} \end{aligned} \quad (8)$$

where $\mathbf{T}$ and $\mathbf{x}$ represent the transformation matrix and the original Cartesian coordinate, respectively; λ is the incident wavelength in the truncated background, and d is the thickness of the PML. The no-jump boundary condition $\mu_r^{-1}(\nabla \times \mathbf{E}_r - \nabla_{\mathbf{x}'} \times \mathbf{E}_r) \times \mathbf{n} = \mathbf{0}$ for the scattering field is imposed on the interface $\partial\Omega$ between Ω_P and Ω and the electric conductor condition $\mathbf{n} \times (\mathbf{E}_r + \mathbf{E}_i) = \mathbf{0}$ is imposed on external boundary Γ_P.

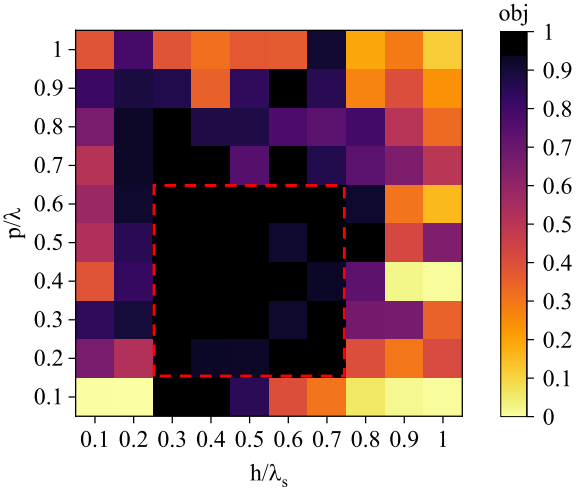

Fig. 5. Converged objective values for different unit periods and dielectric thicknesses with the incident frequency of 10 GHz. The region enclosed by the red dashed line represents the suitable design space.

Due to the periodicity of the metasurface along the x-axis and y-axis, periodic boundary condition is imposed on the boundaries in the x and y directions to reduce the computational cost:

$$\begin{aligned} &\mathbf{E}_r(\mathbf{x} + \mathbf{a}) = \mathbf{E}_r(\mathbf{x}) e^{-j\mathbf{k}\cdot\mathbf{a}}, \\ &\mathbf{n}(\mathbf{x} + \mathbf{a}) \cdot [\nabla \times \mathbf{E}_r(\mathbf{x}) e^{-j\mathbf{k}\cdot\mathbf{a}}] = -e^{-j\mathbf{k}\cdot\mathbf{a}} \mathbf{n}(\mathbf{x}) \cdot [\nabla \times \mathbf{E}_r(\mathbf{x}) e^{-j\mathbf{k}\cdot\mathbf{a}}], \\ &\text{for } \forall \mathbf{x} \in \Gamma_{ps}, \mathbf{x} + \mathbf{a} \in \Gamma_{pd} \end{aligned} \quad (9)$$

where Γ_{ps} and Γ_{pd} are the source and destination boundaries of the periodic boundary pair, respectively; $\mathbf{k}$ and $\mathbf{a}$ represent the wave vector and the lattice vector, respectively.

2.3. Topology optimization

Topology optimization is a computational design methodology that systematically determines the optimal spatial arrangement of material within a given design domain to fulfill specific performance criteria. As demonstrated in Fig. 1c, topology optimization is employed to inversely design the metal patch located on the top layer of the substrate, which is defined as the design domain. The metal patch structure is characterized by the spatial distribution of conductor material within the design domain, defined with the elementwise conductor density, denoted as $\rho_p(i)$ with $0 \le \rho_p \le 1$ for $i = 1, 2, \ldots, N$, where N represents the total number of mesh elements used to discretize the design domain. This material

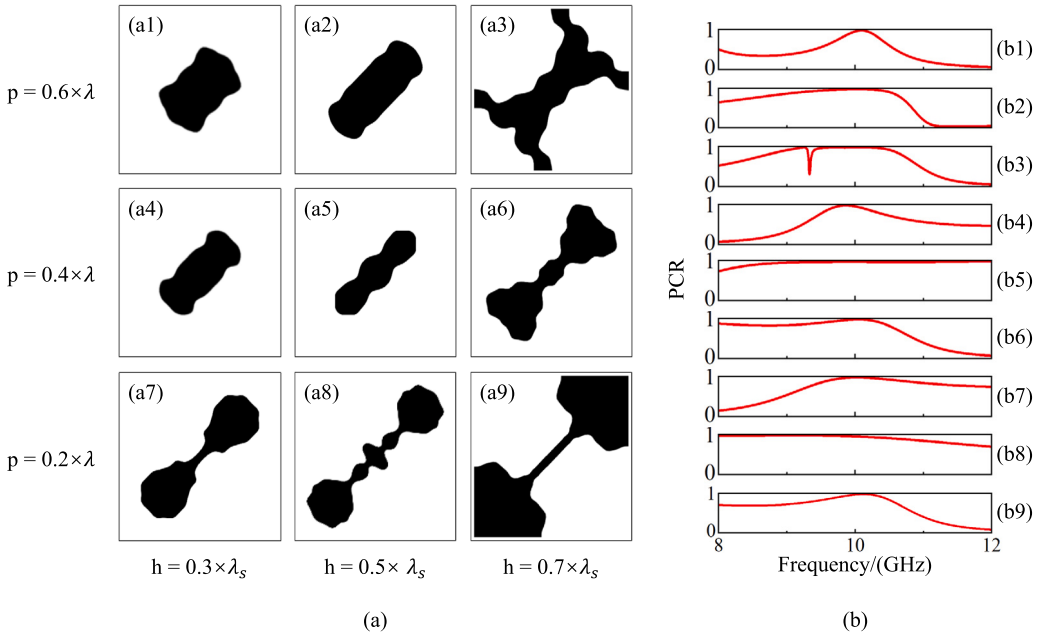

Fig. 6. (a) Topology optimization results for the unit periods of 0.2, 0.4, and 0.6 times of the free-space wavelength, and the dielectric thicknesses of 0.3, 0.5, and 0.7 times of the wavelength in the dielectric medium. (b) PCR values of the obtained structures.

density is obtained by filtering, elementwising and projecting the design variable ρ defined on the design domain.

The primary purpose of filtering the design variable is to ensure the robust evolution of the design and eliminate small structures with sizes comparable to the discretized elements. This filtering process is achieved by solving the following Helmholtz equation [48]:

$$\begin{aligned} &-\nabla\cdot\left(r^2\nabla\rho_f\right)+\rho_f=\rho,\text{in }\Omega_d \\ &\mathbf{n}\cdot\nabla\rho_f=0,\text{on }\partial\Omega_d \end{aligned} \tag{10}$$

where r is the filter radius; ρ is the design variable; and ρ_f is the filtered design variable. By adjusting the filter radius, the minimum feature size of the optimized structure can be controlled.

The material conductivity gradient, resulting from the gradient of the design variable, can cause a violation of the divergence-free condition in the governing equations. Consequently, it is necessary to enforce piecewise uniformity of the design variable within the design domain, such that the conductivity remains constant within each element. An elementwise operation is then performed on the filtered design variable ρ_f to obtain the elementwise variable ρ_e, which represents the average value of the filtered variables within each element [45]. This process can be expressed as

$$\begin{aligned} &\rho_e=\sum_{n=1}^{N}\frac{1}{V_n}\int_{P_n}\rho_f\mathrm{d}\Omega,\text{with} \\ &\begin{cases} V_n=\int_{P_n}1\,\mathrm{d}\Omega, \\ \bigcup_{n=1}^{N}P_n=\Omega, \\ \text{and }P_l\cap P_m=\emptyset\,(l,m=1,2\ldots N,l\neq m) \end{cases} \end{aligned} \tag{11}$$

where N represents the total number of mesh elements used to discretize the design domain.

The elementwise variable is further projected to obtain the material density by using a smoothed approximation of the Heaviside function [49], which serves to eliminate the gray region introduced by the filtering process:

$$\rho_p=\frac{\tanh(\beta\xi)+\tanh\left(\beta(\rho_e-\xi)\right)}{\tanh(\beta\xi)+\tanh(\beta(1-\xi))},\xi\in[0,1],\beta\in[1,+\infty] \tag{12}$$

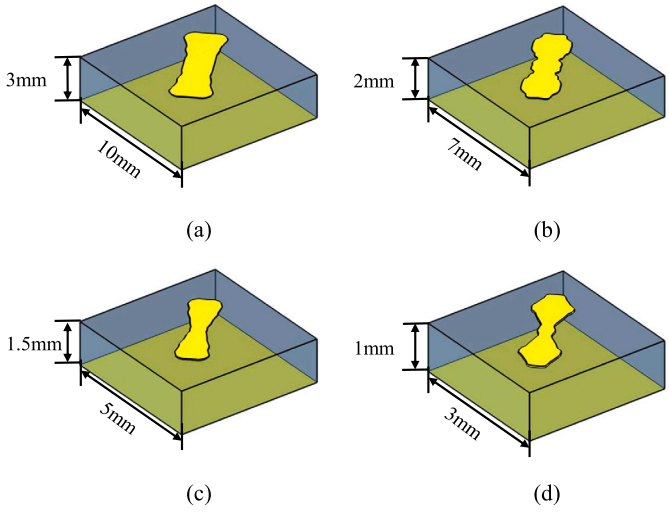

Fig. 7. Topologically optimized unit cells for the target frequency bands of (a) X-band, (b) Ku-band, (c) K-band, and (d) Ka-band, respectively.

where ξ represents the projection point, usually taking the value of 0.5, and β represents the projection slope, with the influence on Heaviside function shown in Fig. 2. When $\beta=1$, the projection has weak effect; as β approaches infinity, the material density almost only takes values of 0 or 1. Specifically, we begin with $\beta=1$, and double it after every 20 iterations until β reaching 2^{10}, to ensure that the final optimization result exhibits clear structural boundaries.

For topology optimization based on the material distribution method, it is necessary to define an interpolation function to map the design variables to material parameters. In the cases where the material parameters differ only slightly, e.g. two dielectric materials with small contrast in dielectric constants, simple linear interpolation can yield satisfactory results [50,51]. However, in our case, due to the significant contrast in conductivity between air and metal, simple linear interpolation is no longer suitable. Here, we adopt the interpolation scheme expressed as [52]

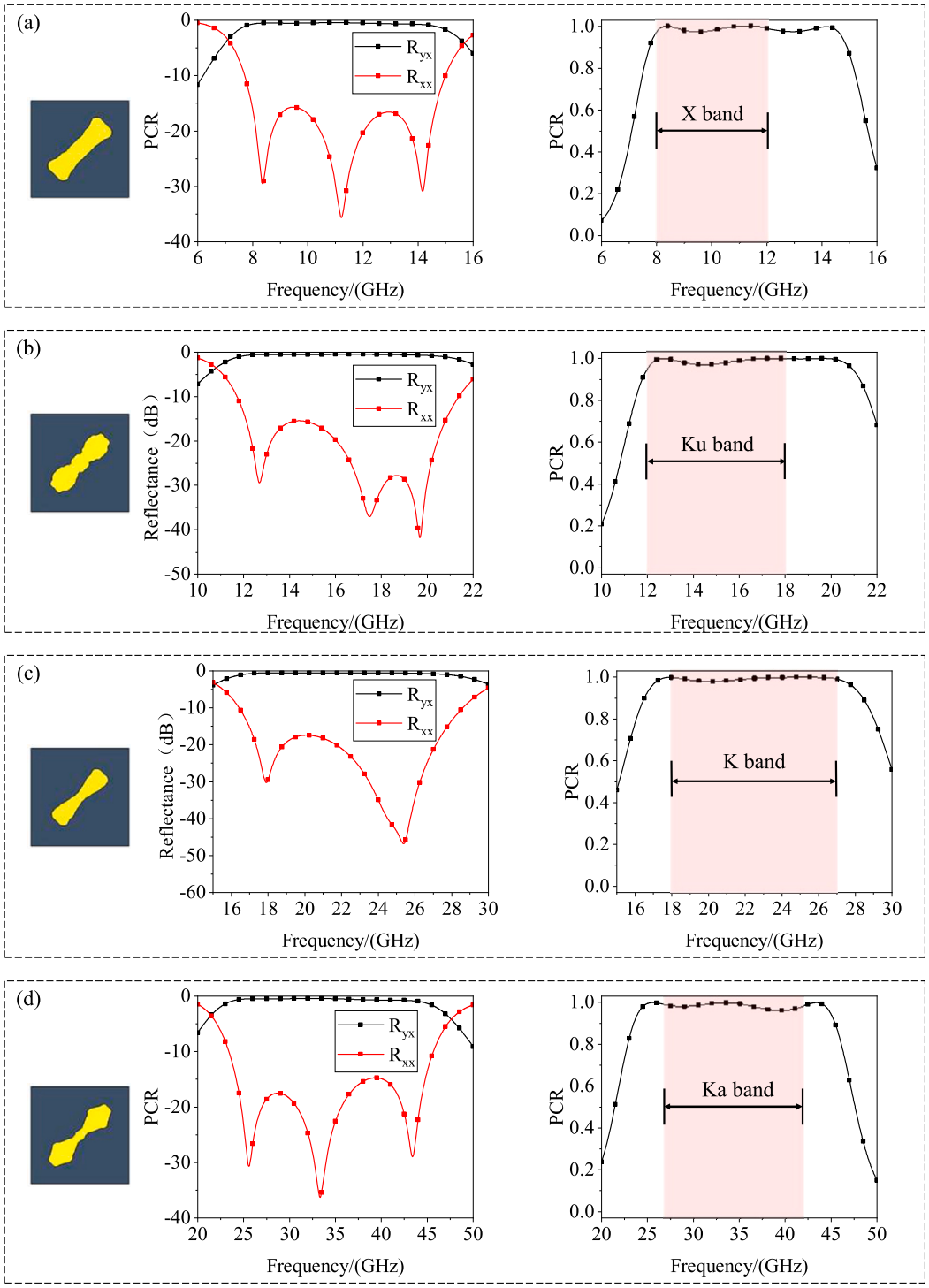

Fig. 8. Reflectance and PCR of the optimized structures for the target frequency bands of (a) X-band, (b) Ku-band, (c) K-band, and (d) Ka-band, respectively, under the condition of x-polarized incident waves.

$$\sigma(\rho_p) = \sigma_{min}\left(\frac{\sigma_{max}}{\sigma_{min}}\right)^{\rho_p} \tag{13}$$

where $\sigma_{min} = 10^{-4}\ S/m$ and $\sigma_{max} = 10^{6}\ S/m$ are the minimum and maximum conductivity values corresponding to air and metal materials, respectively. Strictly, the conductivity of free space should be zero; however, due to numerical considerations, σ_{min} is assigned a small but non-zero value. Nevertheless, this has almost no effect on the EM characteristics of the structure.

For polarization conversion metasurfaces, PCR is the primary performance metric. However, due to the effect of material conductivity on EM wave attenuation, a relatively low cross-polarized reflection coefficient can still lead to a high PCR if the co-polarized reflection component is fully attenuated. As a result, in optimization processes where maximizing PCR serves as the objective function, a large number of undesirable gray values may appear in the optimization process. Although these gray values can be removed during the process of increasing the projection slope, the excessive gray values cause sharp fluctuations in the objective function with each increment in the projection slope, leading to instability of the optimization process. Consequently, the final optimization results are often not acceptable. To avoid this situation, we use maximiz-

ing the normalized cross-polarization reflected energy as the objective function, which not only prevents the PCR from being falsely high, but also makes the optimization problem "self-penalized" [53], i.e. the design variables can naturally converge to the binary distribution. For the case with the incident wave polarized along the x axis, the objective function can be expressed as

$$J = {R_{yx}}^2 = \frac{\int_{\partial\Omega} E_{r,y} E_{r,y}^* \mathrm{d}\Gamma}{\int_{\partial\Omega} \mathbf{E_i} \cdot \mathbf{E_i}^* \mathrm{d}\Gamma} \tag{14}$$

where $\partial\Omega$ represents the interface between Ω_P and Ω; and $*$ represents the conjugate operation of a complex variable.

For the broadband optimization problem, we use a max-min-type objective function. Specifically, we select multiple frequency points within a given frequency band and maximize the minimum objective value among them, to ensure the effectiveness of the optimized structure across the entire frequency band. The objective function can then be expressed as

$$\begin{aligned} &J = \min\ {R_{yx}}^2(\omega) \\ &\text{with } \omega = \omega_{min} + i\frac{\omega_{max} - \omega_{min}}{N-1}, i = 0, 1, ..., N-1 \end{aligned} \tag{15}$$

where N is the total number of sample points selected within the frequency band.

Based on the above discussion, the topology optimization problem for polarization conversion metasurfaces can be constructed as

$$\text{Find } \rho \text{ to maximize } J$$

$$\text{subject to} \begin{cases} \nabla \times [\mu_r^{-1} \nabla \times (\mathbf{E}_r + \mathbf{E}_i)] - k_0^2 \left(\varepsilon_r - \frac{j\sigma}{\omega\varepsilon_0}\right)(\mathbf{E}_r + \mathbf{E}_i) = 0, \text{in } \Omega \\ \nabla \cdot [(\varepsilon_r - \frac{j\sigma}{\omega\varepsilon_0})(\mathbf{E}_r + \mathbf{E}_i)] = 0, \text{in } \Omega \\ -\nabla \cdot \left(r^2 \nabla \rho_f\right) + \rho_f = \rho, \text{in } \Omega_d \end{cases} \tag{16}$$

The topology optimization problem is solved by using a gradient-based algorithm, where the gradient information required for each iteration is obtained by solving the adjoint equations. Based on the finite element solution to the original partial differential equations, the adjoint equations can be efficiently solved to obtain the adjoint variables, which are then used to compute the gradient of the objective function with respect to the design variables. MMA is used to update the design variables. Due to the anisotropy requirement of the polarization conversion metasurfaces, the initial design variables are arranged symmetrically along the 45° diagonal. The stopping criterion is defined as that the change in all design variables is less than 10^{-3} or the maximum number of iterations is reached, where the maximum number of iterations is 220. The flowchart of topology optimization of polarization conversion metasurfaces is illustrated in Fig. 3. The iteration history shown in Fig. 4 demonstrates the efficiency and robustness of the optimization procedure.

3. Results and discussion

To design polarization conversion metasurfaces, the selection of unit period and dielectric layer thickness is critical. To investigate the design space of the unit period and dielectric thickness, a series of metal patches for polarization conversion metasurfaces with varying unit periods and dielectric thicknesses were inversely designed by using the aforementioned topology optimization method, under the condition of an incident frequency of 10 GHz. As shown in the Fig. 5, for unit cells with periods ranging from 0.2 to 0.6 times of the free-space wavelength and dielectric thicknesses ranging from 0.3 to 0.7 times of the dielectric wavelength, the optimization algorithm performs well, with all cases converging to relatively high objective values. Fig. 6 shows a subset of all the optimization results along with the corresponding PCR of the metasurfaces, where each structure achieves a PCR close to 1 at the optimized frequency and therefore nearly complete polarization conversion is achieved.

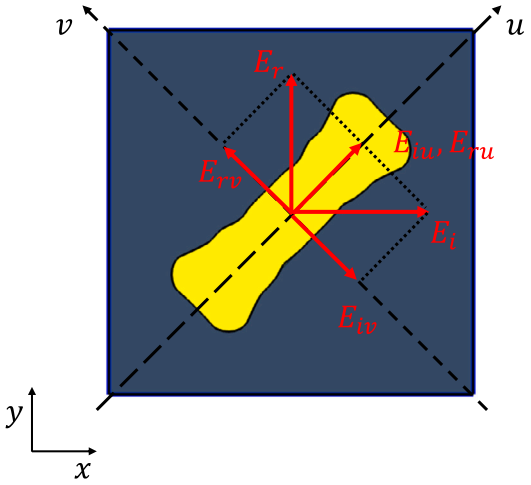

Fig. 9. Schematic diagram of the $u-v$ decomposition of the electric field.

To evaluate the performance of this method in optimizing broadband structures, we conducted the inverse design for multiple polarization conversion metasurface units with target operating frequency bands of X-band (8 − 12 GHz), Ku-band (12 − 18 GHz), K-band (18 − 27 GHz), and Ka-band (27 − 40 GHz). The specific values of the unit period and dielectric thickness are shown in Fig. 7, which were selected based on the design space provided in Fig. 5. The optimization results and the corresponding reflectance and PCR of the metasurfaces are shown in Fig. 8. Compared with the classical design reported in Ref. [54] that achieves polarization conversion functionality within limited bandwidths around two discrete frequencies, the proposed metasurfaces designed via topology optimization enables polarization conversion across a continuous and broad frequency band. Within the target operating frequency bands, the PCR of the metasurfaces consistently exceeds 90%.

To understand the mechanism of polarization conversion shown in Fig. 9, the incident plane EM wave polarized along the x-axis can be decomposed into two perpendicular components as $\mathbf{E}_i = \hat{\mathbf{u}}_\mathbf{u} E_{i,u} e^{j\phi} + \hat{\mathbf{u}}_\mathbf{v} E_{i,v} e^{j\phi}$, and the reflected wave is given by $\mathbf{E}_r = \hat{\mathbf{u}}_\mathbf{u} \mathrm{R}_u E_{i,u} e^{j\phi_u} + \hat{\mathbf{u}}_\mathbf{v} \mathrm{R}_v E_{i,v} e^{j\phi_v}$, where R_u, R_v, ϕ_u and ϕ_v are the reflectance and phase along the u and v-axes, respectively. Due to the anisotropic properties of the metasurface, the phase difference $\Delta\phi$ exists between ϕ_u and ϕ_v. If $\mathrm{R}_u \approx \mathrm{R}_v$ and $\Delta\phi \approx 180°$ are satisfied, the reflected components $E_{r,u}$ and $E_{r,v}$ combine to form a field along the y-axis, resulting in a 90° polarization rotation. To verify this, we numerically simulated the reflectance and phase of the metasurface obtained through the optimization algorithm under the conditions of the incident EM waves polarized along the u-axis and v-axis. The results are shown in Fig. 10, where the reflectance for the u-axis polarized wave is approximately equal to that for the v-axis polarized wave. Additionally, the phase difference within the target frequency band is approximately 180°. This indicates that the metasurface possesses polarization conversion capability over the broad frequency band.

To further investigate broadband polarization conversion, we monitored the surface current distribution of the metasurfaces at the peak PCR frequencies. As shown in Fig. 11, for the optimized structure in the X-band, at the three frequencies where the PCR reaches its peak, the surface currents on the top metal patch and the bottom metal ground plane are antiparallel, and this indicates the magnetic resonance. For the optimized structure in the Ku-band, at the three frequencies corresponding to the PCR peaks, the surface currents on the top metal patch and the bottom metal ground plane are parallel, and this indicates the electric resonance [55]. Similarly, for the optimized structure in the K-band, magnetic resonance occurs at two resonant frequencies, while in the Ka-band, magnetic resonance occurs at 25.58 GHz and 33.34 GHz,

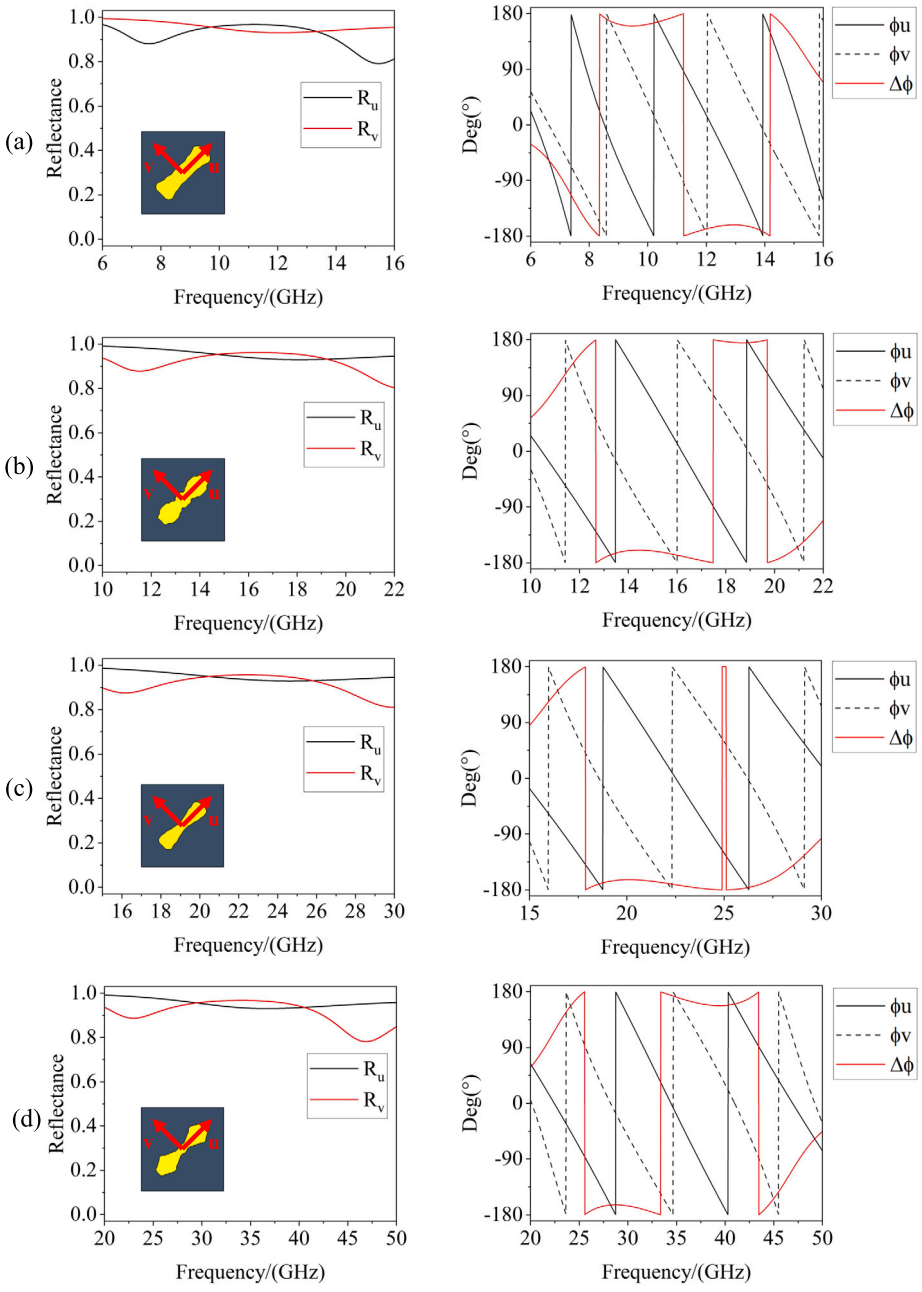

Fig. 10. Reflectance and phase of the optimized structures for the target frequency bands of (a) X-band, (b) Ku-band, (c) K-band, and (d) Ka-band, respectively, under the conditions of *u*-polarized and *v*-polarized incident waves.

and the electric resonance occurs at 43.4 GHz. To elucidate the physical mechanism of polarization conversion functionality in the metasurfaces through electric and magnetic resonances formed by the surface currents, we established the theoretical model illustrated in Fig. 12. In Fig. 12a, the antiparallel currents on the top metal patch and bottom metal ground plane excite the magnetic resonance, generating a magnetic dipole moment m that induces a magnetic field H_{ind} along the v-axis. Through vector decomposition, the $H_{ind,x}$ component exhibits parallel alignment with the incident electric field and it is orthogonal to the incident magnetic field, thereby cross-polarization conversion from x- to y-polarization is enabled. Conversely, the $H_{ind,y}$ component remains perpendicular to the incident electric field while parallel to the incident magnetic field, and this renders it ineffective for the cross-polarization conversion. In Fig. 12b, the parallel currents on the top metal patch and bottom metal ground plane establish an electric resonance, and they generate the induced electric field E_{ind} which can decompose into $E_{ind,x}$ and $E_{ind,y}$ components. The $E_{ind,y}$ component, orthogonal to the incident electric field and parallel to the incident magnetic field, facilitates x-to-y polarization conversion through the cross-coupling interactions. However, the $E_{ind,x}$ component aligns parallel with the incident electric field while remaining perpendicular to the incident magnetic field, thereby it contributes negligibly to the cross-polarization conversion process. Due to the multi-resonance effect, the topologically optimized structures can operate effectively over a broad frequency band.

To validate the accuracy of simulation results, experimental samples were fabricated using printed circuit board (PCB) technology. As illustrated in Fig. 13c, d, e, and f, the structural units were periodically arranged to form a metal-dielectric-metal tri-layer configuration, where copper patterns were etched onto an FR4 substrate with a metallic ground plane. The experimental setup, depicted in Fig. 13a, employed two linearly polarized horn antennas and a vector network analyzer

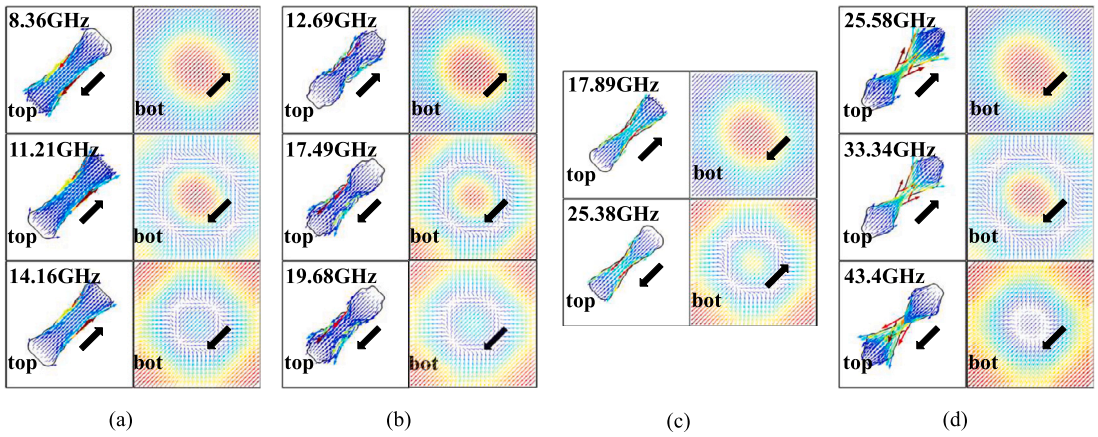

Fig. 11. Surface current distributions at the resonant frequencies on the top metal patch and the bottom metal reflector of the optimized structures for the target frequency bands of (a) X-band, (b) Ku-band, (c) K-band, and (d) Ka-band, respectively.

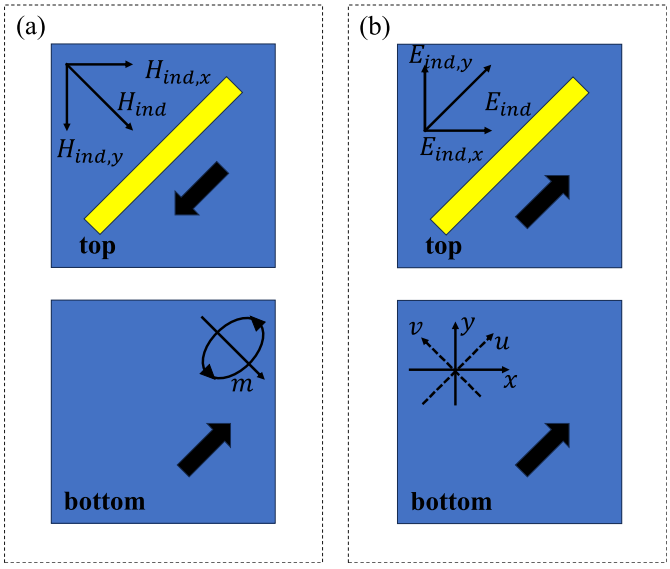

Fig. 12. Theoretical model of (a) magnetic resonance and (b) electric resonance.

(VNA) in an anechoic chamber to transmit/receive linearly polarized waves and analyze reflection coefficients. The PCR in the target frequency band was calculated from measured co-polarized and cross-polarized reflection coefficients. Comparative analysis between experimental and simulated PCR results, presented in Fig. 13g, h, i, and j, demonstrates good agreement with minor discrepancies. These observed discrepancies could be attributed to fabrication tolerances, finite sample dimensions, and measurement system uncertainties.

4. Conclusions

In this article, we present a gradient-based topology optimization method for the inverse design of polarization conversion metasurfaces, where topology optimization is implemented by using the material distribution approach. Through the inverse design of polarization conversion metasurfaces with varying unit periods and dielectric layer thicknesses under a 10 GHz incident frequency, we identified the design space for unit periods ranging from 0.2 to 0.6 times of the free-space wavelength and dielectric thicknesses from 0.3 to 0.7 times of the wavelength in the dielectric medium. To ensure the optimized structure performs effectively across a wide bandwidth, we adopted a max-min-type objective function, selecting multiple frequency points within a given frequency band and maximizing the minimum objective value among them. Furthermore, the inverse design was carried out for metasurfaces with target operating bands in the X-band, Ku-band, K-band, and Ka-band, achieving PCR exceeding 90% within the target frequency bands. Additionally, we explored their broadband polarization conversion mechanisms through theoretical analysis based on surface current distributions. The topologically optimized metasurfaces are experimentally verified and remarkable agreement is exhibited between the numerical and experimental results. This method can provide significant improvement for the design of broadband polarization conversion metasurfaces and shows great potential for applications in the design of other types of metasurfaces, such as frequency-selective metasurfaces and absorbing metasurfaces.

CRediT authorship contribution statement

Honglin Zhong: Writing – review & editing, Writing – original draft, Methodology, Formal analysis, Data curation. **Bowen Li:** Validation, Methodology, Formal analysis. **Yu Lin:** Resources, Methodology, Investigation. **Yeming Han:** Formal analysis, Conceptualization. **Chengmiao Wang:** Investigation. **Wei Sha:** Methodology, Investigation. **Jan G. Korvink:** Supervision, Conceptualization. **Yongbo Deng:** Writing – review & editing, Writing – original draft, Validation, Supervision, Resources, Project administration, Methodology, Funding acquisition, Conceptualization.

Declaration of competing interest

The authors declare that they have no known competing financial interests or personal relationships that could have appeared to influence the work reported in this paper.

Acknowledgements

This work was supported by the National Natural Science Foundation of China (No. 51875545), Science and Technology Development Plan of Jilin Province (No. SKL202302020), CAS Project for Young Scientists in Basic Research (No. YSBR-066), the Innovation Grant of Changchun Institute of Optics, Fine Mechanics and Physics (CIOMP), EU2020 FET grant (TiSuMR, 737043), the DFG under grant KO 1883/20-1 Metacoils, funding within their framework of the German Excellence Intitiative under grant EXC 2082 “3D Matter Made to Order”, and from the VirtMat initiative “Virtual Materials Design”.

Data availability

Data will be made available on request.

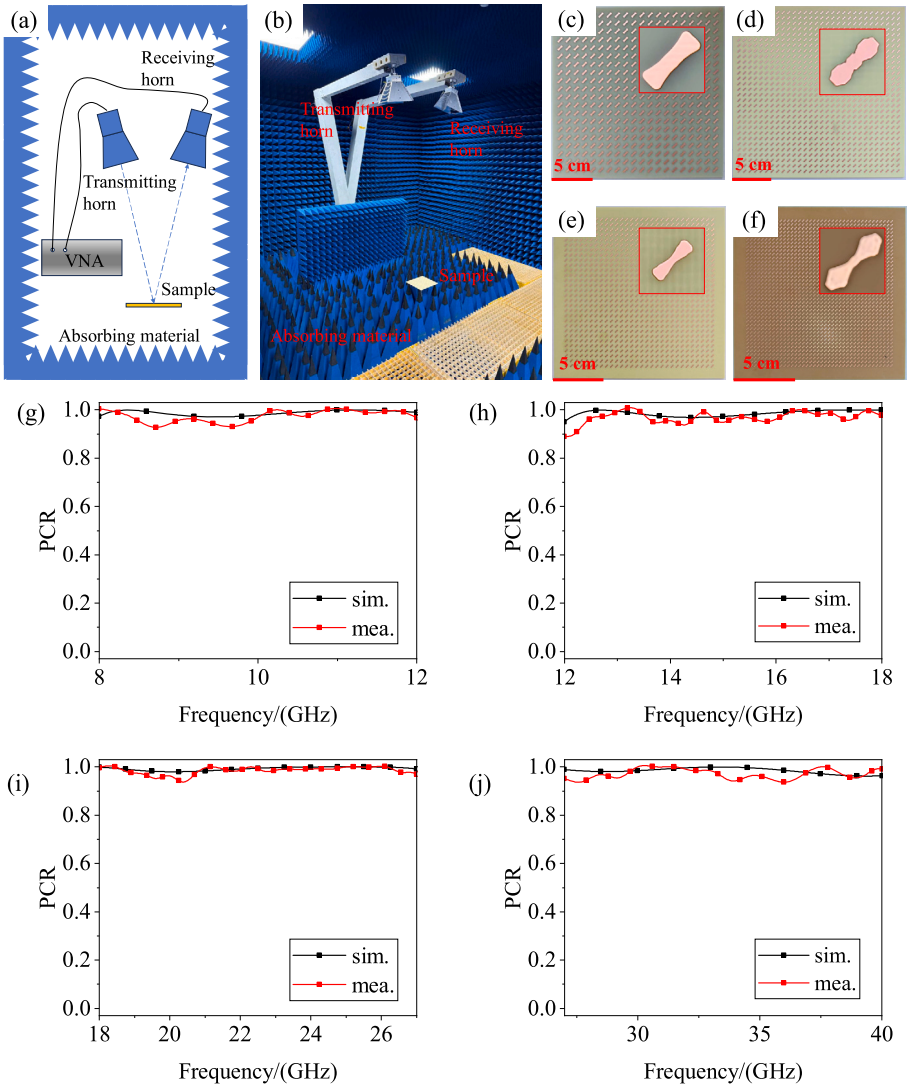

Fig. 13. Measurement setup and the test results of the metasurfaces. (a) Sketch of the measuring platform. (b) Configuration of the measurement setup. (c) Sample of metasurface targeting the X-band, characterized by a polarizer array with 20×20 elements and overall dimensions of $210 \times 210 \times 3$ mm^3. (d) Sample of metasurface targeting the Ku-band, characterized by a polarizer array with 30×30 elements and overall dimensions of $220 \times 220 \times 2$ mm^3. (e) Sample of metasurface targeting the K-band, characterized by a polarizer array with 30×30 elements and overall dimensions of $170 \times 170 \times 1.5$ mm^3. (f) Sample of metasurface targeting the Ka-band, characterized by a polarizer array with 40×40 elements and overall dimensions of $140 \times 140 \times 1$ mm^3. (g), (h), (i), (j) show the simulated and measured PCR of the metasurfaces targeting the X-band, Ku-band, K-band, and Ka-band, respectively.

References

[1] Caili Guo, et al., Advances on exploiting polarization in wireless communications: channels, technologies, and applications, IEEE Commun. Surv. Tutor. 19 (1) (2016) 125–166.

[2] Milorad Cvijetic, Ivan Djordjevic, Advanced Optical Communication Systems and Networks, Artech House, 2013.

[3] Shijie Zhang, Zongwen Li, Fei Xing, Review of polarization optical devices based on graphene materials, Int. J. Mol. Sci. 21 (5) (2020) 1608.

[4] Yuttana Intaravanne, Xianzhong Chen, Recent advances in optical metasurfaces for polarization detection and engineered polarization profiles, Nanophotonics 9 (5) (2020) 1003–1014.

[5] Sampurna De, A.A. Bazil Raj, A survey on photonics technologies for radar applications, J. Opt. 52 (1) (2023) 90–119.

[6] Hongya Chen, et al., Ultra-wideband polarization conversion metasurfaces based on multiple plasmon resonances, J. Appl. Phys. 115 (2014) 15.

[7] H.L. Zhu, et al., Linear-to-circular polarization conversion using metasurface, IEEE Trans. Antennas Propag. 61 (9) (2013) 4615–4623.

[8] Hong-Ya Chen, et al., Broadband perfect polarization conversion metasurfaces, Chin. Phys. B 24 (1) (2015) 014201.

[9] Ping Yu, Jianxiong Li, Na Liu, Electrically tunable optical metasurfaces for dynamic polarization conversion, Nano Lett. 21 (15) (2021) 6690–6695.

[10] Ying Liu, et al., Wideband RCS reduction of a slot array antenna using polarization conversion metasurfaces, IEEE Trans. Antennas Propag. 64 (1) (2015) 326–331.

[11] Shuai Wang, et al., Arbitrary polarization conversion dichroism metasurfaces for all-in-one full Poincaré sphere polarizers, Light: Sci. Appl. 10 (1) (2021) 24.

[12] Chun Ni, et al., Design of frequency- and polarization-reconfigurable antenna based on the polarization conversion metasurface, IEEE Antennas Wirel. Propag. Lett. 17 (1) (2017) 78–81.

[13] Shuyun Teng, et al., Conversion between polarization states based on a metasurface, Photon. Res. 7 (3) (2019) 246–250.

[14] Yongjun Huang, et al., Polarization conversion of metasurface for the application of wide band low-profile circular polarization slot antenna, Appl. Phys. Lett. 109 (2016) 5.

[15] He-Xiu Xu, et al., Dynamical control on helicity of electromagnetic waves by tunable metasurfaces, Sci. Rep. 6 (1) (2016) 27503.

[16] He-Xiu Xu, et al., Janus reflective polarization-division metadevices with versatile functions, IEEE Trans. Microw. Theory Tech. 71 (8) (2023) 3273–3283.

[17] He-Xiu Xu, et al., Multifunctional microstrip array combining a linear polarizer and focusing metasurface, IEEE Trans. Antennas Propag. 64 (8) (2016) 3676–3682.

[18] Sukumar Vidhya, Madurakavi Karthikeyan, Ultra-wide band and high efficient polarization converting metasurface employing bell-shaped unit cell for rcs reduction, Results Eng. 24 (2024) 103342.

[19] Md Bellal Hossain, et al., A coding based metasurface absorber with triple circular ring resonator for broadband RCS reduction and high EMI shielding effectiveness, Results Eng. 21 (2024) 101791.

[20] Babar Kamal, et al., Design and experimental analysis of dual-band polarization converting metasurface, IEEE Antennas Wirel. Propag. Lett. 20 (8) (2021) 1409–1413.

[21] Michele Borgese, et al., Optimal design of miniaturized reflecting metasurfaces for ultra-wideband and angularly stable polarization conversion, Sci. Rep. 8 (1) (2018) 7651.
[22] Bilawal Khan, et al., Design and experimental analysis of dual-band polarization converting metasurface for microwave applications, Sci. Rep. 10 (1) (2020) 15393.
[23] Yan Shi, Hao Xuan Meng, Hua Jie Wang, Polarization conversion metasurface design based on characteristic mode rotation and its application into wideband and miniature antennas with a low radar cross section, Opt. Express 29 (5) (2021) 6794–6809.
[24] Omar A.M. Abdelraouf, et al., Recent advances in tunable metasurfaces: materials, design, and applications, ACS Nano 16 (9) (2022) 13339–13369.
[25] Emiliano Cortés, et al., Optical metasurfaces for energy conversion, Chem. Rev. 122 (19) (2022) 15082–15176.
[26] Oscar Quevedo-Teruel, et al., Roadmap on metasurfaces, J. Opt. 21 (7) (2019) 073002.
[27] Zin Lin, et al., Topology optimization of freeform large-area metasurfaces, Opt. Express 27 (11) (2019) 15765–15775.
[28] Evan W. Wang, et al., Robust design of topology-optimized metasurfaces, Opt. Mater. Express 9 (2) (2019) 469–482.
[29] Borui Wu, et al., Equivalent-circuit-intervened deep learning metasurface, Mater. Des. 218 (2022) 110725.
[30] Qi Yuan, et al., Centrosymmetric topology optimization design achieves ultra-broadband polarization conversion and its further application, J. Phys. D, Appl. Phys. 53 (33) (2020) 335001.
[31] Sai Sui, et al., Symmetry-based coding method and synthesis topology optimization design of ultra-wideband polarization conversion metasurfaces, Appl. Phys. Lett. 109 (2016) 1.
[32] Ya-Jie Zhang, et al., Ultra-broadband and wide-angle reflective terahertz polarization conversion metasurface based on topological optimization, Chin. Phys. B 33 (10) (2024) 104210.
[33] Ole Sigmund, On the usefulness of non-gradient approaches in topology optimization, Struct. Multidiscip. Optim. 43 (2011) 589–596.
[34] S.Y. Wang, Kang Tai, Michael Yu Wang, An enhanced genetic algorithm for structural topology optimization, Int. J. Numer. Methods Eng. 65 (1) (2006) 18–44.
[35] David Guirguis, et al., Evolutionary black-box topology optimization: challenges and promises, IEEE Trans. Evol. Comput. 24 (4) (2019) 613–633.
[36] Mats Gustafsson, Sailing He, An optimization approach to two-dimensional time domain electromagnetic inverse problems, Radio Sci. 35 (2) (2000) 525–536.
[37] Anders Bondeson, Yongtao Yang, Per Weinerfelt, Shape optimization for radar cross sections by a gradient method, Int. J. Numer. Methods Eng. 61 (5) (2004) 687–715.
[38] Natalia K. Nikolova, Helen W. Tam, Mohamed H. Bakr, Sensitivity analysis with the FDTD method on structured grids, IEEE Trans. Microw. Theory Tech. 52 (4) (2004) 1207–1216.
[39] Sougata Mukherjee, et al., Accelerating large-scale topology optimization: state-of-the-art and challenges, Arch. Comput. Methods Eng. (2021) 1–23.
[40] Subhayan De, et al., Topology optimization under uncertainty using a stochastic gradient-based approach, Struct. Multidiscip. Optim. 62 (2020) 2255–2278.
[41] Rajan Agrahari, et al., Pixelated metasurfaces for linear-polarization conversion and absorption, J. Electromagn. Waves Appl. 36 (7) (2022) 1008–1019.
[42] Shuguang Fang, et al., Dual-function flexible metasurface for absorption and polarization conversion and its application for radar cross section reduction, J. Appl. Phys. 131 (2022) 13.
[43] Kun Li, et al., A circularly polarized high-gain antenna with low RCS over a wideband using chessboard polarization conversion metasurfaces, IEEE Trans. Antennas Propag. 65 (8) (2017) 4288–4292.
[44] Yongbo Deng, Adjoint Topology Optimization Theory for Nano-Optics, Springer, 2022.
[45] Yongbo Deng, Jan G. Korvink, Topology optimization for three-dimensional electromagnetic waves using an edge element-based finite-element method, Proc. R. Soc. A, Math. Phys. Eng. Sci. 472 (2189) (2016) 20150835.
[46] Jean-Pierre Berenger, A perfectly matched layer for the absorption of electromagnetic waves, J. Comput. Phys. 114 (2) (1994) 185–200.
[47] Jian-Ming Jin, The Finite Element Method in Electromagnetics, John Wiley & Sons, 2015.
[48] Boyan Stefanov Lazarov, Ole Sigmund, Filters in topology optimization based on Helmholtz-type differential equations, Int. J. Numer. Methods Eng. 86 (6) (2011) 765–781.
[49] Fengwen Wang, Boyan Stefanov Lazarov, Ole Sigmund, On projection methods, convergence and robust formulations in topology optimization, Struct. Multidiscip. Optim. 43 (2011) 767–784.
[50] Yupei Wei, et al., High-efficiency achromatic metalens in long-wavelength infrared composed of topologically optimized building blocks, Opt. Mater. 151 (2024) 115314.
[51] Lijuan Zhang, et al., High-efficiency achromatic metalens topologically optimized in the visible, Nanomaterials 13 (5) (2023) 890.
[52] Aycan Erentok, Ole Sigmund, Topology optimization of sub-wavelength antennas, IEEE Trans. Antennas Propag. 59 (1) (2010) 58–69.
[53] Emadeldeen Hassan, Eddie Wadbro, Martin Berggren, Topology optimization of metallic antennas, IEEE Trans. Antennas Propag. 62 (5) (2014) 2488–2500.
[54] Jiaming Hao, et al., Manipulating electromagnetic wave polarizations by anisotropic metamaterials, Phys. Rev. Lett. 99 (6) (2007) 063908.
[55] Jiangfeng Zhou, et al., Unifying approach to left-handed material design, Opt. Lett. 31 (24) (2006) 3620–3622.